
Measured Hot-Electron Intensity Thresholds Quantified by a Two-Plasmon–Decay Resonant Common-Wave Gain in Various Experimental Configurations

Introduction

In inertial confinement fusion (ICF), a spherical capsule is imploded using multiple laser beams to produce an energetic fusion reaction by compressing nuclear fuel to high densities and temperatures.¹ In the direct-drive scheme,² the capsule is uniformly illuminated by overlapping beams, and in the indirect-drive scheme,³ the laser beams are first converted into x rays that then illuminate the capsule. In both schemes, the laser beams can drive the two-plasmon–decay (TPD) instability.^{4–8} When TPD is driven strongly, an extended spectrum of large-amplitude electron plasma waves (EPW's) is generated that accelerates electrons to high energies (~ 100 keV) (Refs. 9–12). These electrons can deposit their energy in the fuel (preheat), reducing the compression efficiency and potentially inhibiting ICF ignition. Although no experiments have definitively measured the effects of preheat, hydrodynamic simulations that include an *ad hoc* hot-electron model indicate low-adiabat ignition designs can survive $\sim 0.1\%$ of laser energy converted into hot electrons and coupled to the fusion fuel.¹³

The TPD instability results from the decay of an electromagnetic wave into two electron plasma waves.^{4,5} Phase matching, energy conservation, and the dispersion relations of the waves limit the instability to a small region near the quarter-critical density surface. Stability calculations of a single linearly polarized electromagnetic wave show that the absolute threshold of the instability is proportional to $I_s L_n / T_e$, where I_s is the laser-beam intensity, L_n is the plasma density scale length, and T_e is the electron temperature of the plasma at the quarter-critical density.⁶ More-recent particle-in-cell (PIC) simulations have shown the importance of convective mode in the nonlinear stage that also depends on $I_s L_n / T_e$ (Ref. 14). Multibeam experiments have shown that hot-electron production scales with the overlapped vacuum laser-beam intensity (I_{OVP}) (Ref. 15) independent of the number of beams used. This scaling is not expected if the laser beams drive TPD independently. To explain these results, a multibeam model was proposed where different laser beams share a common electron plasma wave.^{16,17} Recent experiments at the Omega Laser Facility^{18,19} showed that the overlapped intensity threshold for hot-electron

generation depends on the laser-beam and target geometries.²⁰ A model that calculates the homogeneous, multibeam, TPD growth rate shows that beams that share the same angle with respect to the common-wave vector can couple through the resonant common electron plasma wave and that this coupling occurs in the region in k space bisecting the laser beams.²¹ In this common-wave region, the TPD growth rate depends on the geometry and the polarization of the laser beams.

This article reports on the measured hot-electron fraction generated by TPD in planar experiments using one to four linearly polarized beams, 18 beams with polarization smoothing, and, in spherical experiments, 60 beams with polarization smoothing. The overlapped intensity threshold for hot-electron generation is different for each experimental configuration. These measured thresholds are compared with convective gains calculated with the resonant common-wave model.

The following sections describe (1) the various experimental configurations; (2) the experimental results, where the overlapped intensity threshold for hot-electron generation is observed to be different for the various experimental configurations; and (3) the multibeam TPD resonant common-wave growth rate for linearly polarized beams and beams with polarization smoothing. Next, the common-wave gain is shown to be consistent with observed variations in the TPD thresholds, followed by the conclusions.

Experimental Setup

The experiments discussed here were designed to measure the intensity thresholds for the production of hot electrons while varying different parameters in the common-wave gain. On OMEGA EP,¹⁹ the hot-electron fraction was measured in planar geometry as a function of the laser energy for one-, two-, and four-beam configurations to study the variation of the hot-electron production with a maximum normalized growth rate that depends on the polarization and geometry of the laser beams. The four-beam results were compared to OMEGA planar experiments, where 18 beams distributed in three cones were used to study the variation in the hot-electron production

with the number of beams that contribute to the common-wave TPD. The planar experiments are compared to OMEGA experiments in spherical geometry to measure the variation in the hot-electron production with the plasma parameters.

1. Laser Setup

a. OMEGA EP planar geometry. In the OMEGA EP experiments, four vertically polarized 351-nm beams intersected the target at an angle of 23° with respect to the target normal [Fig. 133.34(a)]. The focal spots of the beams were spatially overlapped to within $20\ \mu\text{m}$. The beams used 2-ns flattop laser pulses that were co-timed to within 50 ps. Two sets of distributed phase plates (DPP's)²² were used [860- μm full width at half maximum (FWHM) for Beams 1 and 2 and 800- μm FWHM for Beams 3 and 4] to produce an ~ 1 -mm-diam, ninth-order super-Gaussian intensity profile. A maximum single-beam energy of 2.0 kJ (2.6 kJ) was used on Beams 1 and 2 (3 and 4), resulting in peak single-beam intensities $I_{\text{max}} = 1.8 \times 10^{14}\ \text{W/cm}^2$ ($I_{\text{max}} = 2.6 \times 10^{14}\ \text{W/cm}^2$). Experiments were performed using one beam; two beams in a horizontal configuration (Beams 1 and 4), vertical configuration (Beams 1 and 3), and diagonal configuration (Beams 1 and 2); and four beams [Fig. 133.34(a)].

b. OMEGA planar geometry. In the OMEGA planar experiments, 18 beams at a wavelength of 351 nm intersected the

target in three cones of six beams at angles of 23° , 48° , and 63° with respect to the target normal [Fig. 133.34(b)]. The beams were spatially overlapped to within $20\ \mu\text{m}$. The beams used 2-ns flattop laser pulses that were co-timed to within 10 ps. All beams were smoothed by polarization smoothing (PS)²³ and DPP's (710- μm FWHM) to produce an ~ 1 -mm-diam, fourth-order super-Gaussian intensity profile. The single-beam energy ranged from 240 J to 380 J, providing a peak single-beam intensity ranging from $3.4 \times 10^{13}\ \text{W/cm}^2$ to $5.4 \times 10^{13}\ \text{W/cm}^2$.

c. OMEGA spherical geometry. In the OMEGA spherical experiments, 60 laser beams at 351 nm smoothed by PS and DPP's (710- μm FWHM) uniformly illuminated an 860- μm -diam spherical target [Fig. 133.34(c)]. The beams were pointed with an accuracy of $20\ \mu\text{m}$. The beams used 1-ns flattop laser pulses that were co-timed to within 10 ps. The 60 laser beams used a total energy of 13 kJ to 29.5 kJ to produce a spherically symmetric illumination of the target. The peak single-beam intensity was varied from $5 \times 10^{13}\ \text{W/cm}^2$ to $1.2 \times 10^{14}\ \text{W/cm}^2$.

2. Targets

a. Planar geometry. For the planar experiments on both OMEGA and OMEGA EP, the laser beams illuminated a 30- μm -thick CH layer deposited on 30 μm of Mo and backed with an additional 30 μm of CH. Hydrodynamic simulations using the two-dimensional (2-D) code *DRACO*²⁴ indicated that

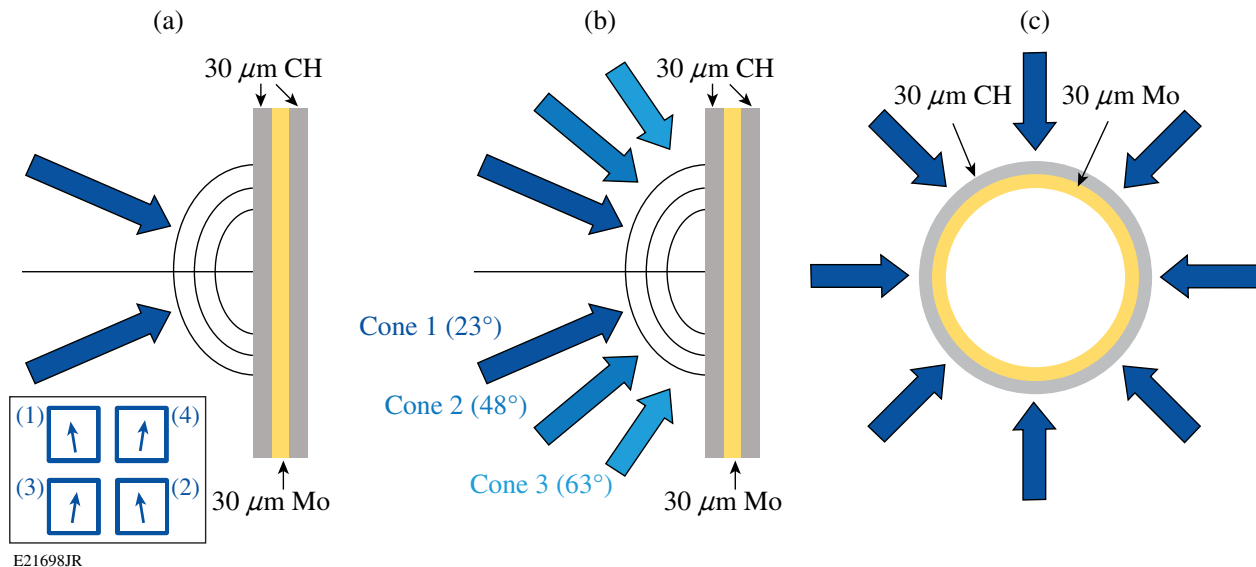


Figure 133.34

Schematic of the laser-beam configurations on (a) OMEGA EP, (b) OMEGA (planar geometry), and (c) OMEGA (spherical geometry). In OMEGA EP experiments, the polarizations of the beams are 8° from vertical [inset in (a)], and in OMEGA experiments, the beams used polarization smoothing.

the laser light interacted with the first layer, producing a CH plasma with density and temperature profiles that depended (for each configuration) only on the overlapped laser intensity. For the experimental conditions presented here, the hydrodynamic profiles near quarter-critical density reached steady state after about 1.5 ns. After this time, the calculated quantity $I_{\text{ovr,q}}L_{\text{n,q}}/T_{\text{e,q}}$ varied by less than 10% at the quarter-critical density (the subscript “q” refers to quantities at the quarter-critical density surface).

For the OMEGA EP experiments, the overlapped laser intensity was increased from $1.5 \times 10^{14} \text{ W/cm}^2$ to $7 \times 10^{14} \text{ W/cm}^2$, the density scale length ($L_{\text{n,q}}$) increased from 260 μm to 360 μm , and the electron temperature ($T_{\text{e,q}}$) increased from 1.5 keV to 2.5 keV; the ratio $L_{\text{n,q}}/T_{\text{e,q}}$ was nearly constant over this intensity range ($\approx 160 \mu\text{m/keV}$). The laser intensity at quarter-critical density was about half the vacuum intensity.

For the OMEGA planar experiments, the overlapped laser intensity was increased from $4 \times 10^{14} \text{ W/cm}^2$ to $6.5 \times 10^{14} \text{ W/cm}^2$, the density scale length ($L_{\text{n,q}}$) increased from 260 μm to 320 μm , and the electron temperature ($T_{\text{e,q}}$) increased from 2 keV to 2.4 keV; the ratio $L_{\text{n,q}}/T_{\text{e,q}}$ was nearly constant over this intensity range ($\approx 135 \mu\text{m/keV}$). The overlapped laser intensity at quarter-critical density was about half the vacuum overlapped intensity.

b. Spherical geometry. In the spherical experiments, the laser beams illuminated an 800- μm -diam, 30- μm -thick Mo shell coated with 30 μm of CH. Hydrodynamic simulations using the one-dimensional (1-D) code *LILAC*²⁵ showed that the laser light interacted only with the CH layer and the hydrodynamic profiles near quarter-critical density reached a steady state after about 0.5 ns. After this time, the calculated quantity $I_{\text{ovr,q}}L_{\text{n,q}}/T_{\text{e,q}}$ varied by less than 10%, where $I_{\text{ovr,q}} \equiv P_{\text{L,q}}/4\pi R_{\text{q}}^2$, $P_{\text{L,q}}$ is the laser power at the quarter-critical-density surface, and R_{q} is the radius of the quarter-critical-density surface. When the overlapped laser intensity was increased from $5 \times 10^{14} \text{ W/cm}^2$ to $12 \times 10^{14} \text{ W/cm}^2$, the density scale length ($L_{\text{n,q}}$) increased from 120 μm to 140 μm and the electron temperature ($T_{\text{e,q}}$) increased from 2.1 keV to 2.2 keV; the ratio $L_{\text{n,q}}/T_{\text{e,q}}$ was nearly constant over this intensity range ($\approx 60 \mu\text{m/keV}$). The overlapped laser intensity at quarter-critical density (570 μm) was about half the overlapped vacuum intensity.

3. Diagnostics

Two principal diagnostics were used to determine the amount of laser energy converted to hot electrons: an x-ray spectrometer

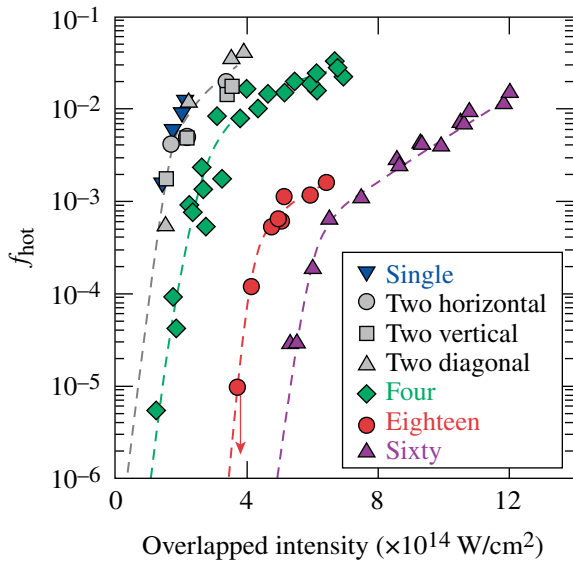
(XRS)^{26–28} and a hard x-ray detector (HXRD).²⁹ Monte Carlo simulations using the code *EGSnrc*³⁰ were used to determine the total hot-electron energy (E_{e}) given the measured hard x-ray temperature and the total energy in the K_{α} emission.²⁶

a. X-ray spectrometer. The XRS measures the energy emitted into the Mo K_{α} emission line ($E_{\text{K}_{\alpha}}$) using an absolutely calibrated planar LiF crystal spectrometer that views the target from the laser’s incident side at an angle of 63° from the target normal²⁶ on OMEGA EP, 37.4° from the target normal on OMEGA planar experiments, and along the target normal for spherical experiments. The Monte Carlo simulations show that electrons with energies less than 120 keV are stopped in the Mo. The 17.5-keV Mo K_{α} line is sufficiently energetic so that photoexcitation from the 2.5-keV coronal plasma region does not contribute to the K_{α} -emission measurement.

b. Hard x-ray detector. The hard x-ray detector consists of a three-channel filtered scintillator array that measures the x-ray radiation generated by the hot electrons in the Mo above ~ 40 keV, ~ 60 keV, and ~ 80 keV (Ref. 29). The hard x-ray detector views the back of the target at an angle of 40° from the target normal on OMEGA EP and 42° from the target normal on OMEGA planar experiments. The hard x-ray temperature is estimated using the exponentially decreasing x-ray energies measured by the three channels. The relative error in the measurement of the slope (T_{rad}) in the hard x-ray spectrum is 20%. Monte Carlo simulations indicate that the hard x-ray temperature is a good measure of the hot-electron temperature T_{hot} ($T_{\text{rad}} \simeq T_{\text{hot}}$) (Ref. 26).

Experimental Results

Figure 133.35 shows that for all configurations tested, the hot-electron fraction defined as the fraction of laser energy converted to hot electrons (f_{hot}) increases exponentially with the overlapped vacuum laser-beam intensities and, at high intensities, the increase is much slower. The rapid increase in hot-electron production at low intensities is used to determine an intensity threshold defined as the overlapped intensity when the hot-electron fraction is equal to 10^{-4} (near the detector threshold). For one and two linearly polarized beams in the horizontal, vertical, and diagonal configuration (OMEGA EP planar geometry), a similar evolution with the overlapped-laser-beam intensity is measured and a hot-electron-production threshold of $I_{\text{th}} \sim 10^{14} \text{ W/cm}^2$ is inferred. For the four-beam configuration (OMEGA EP planar geometry), the threshold dependence on the overlapped intensity is increased by a factor of 2 and a threshold of $I_{\text{th}} \sim 2 \times 10^{14} \text{ W/cm}^2$ is measured. A factor-of-2 further increase in the



E21699JR

Figure 133.35

Hot-electron fraction (f_{hot}) as a function of vacuum overlapped laser intensity. Single, two, and four correspond to OMEGA EP planar experiments where the beams are linearly polarized; 18 (60) corresponds to OMEGA planar (spherical) experiments where the beams have polarization smoothing. The dashed lines are drawn to guide the eye. In each case, the overlapped intensity at quarter-critical density is about half the vacuum overlapped intensity. For the 18-beam configuration, at an overlapped intensity of 4×10^{14} W/cm², the signal was lower than the diagnostic detection threshold (red arrow).

intensity threshold ($I_{\text{th}} \sim 4.2 \times 10^{14}$ W/cm²) is observed for the 18-beam configuration (OMEGA planar geometry). In spherical geometry, the intensity threshold is $\sim 3\times$ higher than for the four-beam configuration ($I_{\text{th}} \sim 6 \times 10^{14}$ W/cm²). These data underline the fact that the hot-electron intensity threshold depends strongly on the experimental configuration.

The measured rapid growth of the hot-electron fraction with the laser intensity is consistent with the exponential growth expected for convective TPD. This suggests that nonlinear mechanisms that may occur at low intensities are not sufficient to saturate the growth of the electron plasma waves. At higher intensities, the increase in the hot-electron fraction with laser intensity is reduced, suggesting that the TPD growth is affected by a nonlinear saturation mechanism.

Time-resolved data obtained with HXRD show that the hot-electron production occurs toward the end of the laser pulse. The instantaneous hot-electron fraction at the end of the pulse is typically a factor of ~ 2 higher than the value aver-

aged over the entire pulse.¹² These hot-electron measurements account for all electrons produced. In a fusion experiment, the hot-electron energy coupled to the core is expected to be significantly reduced by the divergence of the electrons angle and the variation in their energy.

Common-Wave Modeling

In this section, the resonant-TPD growth rate is calculated for multiple laser beams. The growth rate is shown to depend on the beam geometry, the beam polarization, and the sum of the intensities of the beams that share the same angle with the common electron plasma wave vector. For multiple laser beams with polarization smoothing, the maximum normalized growth rate is shown to be constant and independent of the geometry of the beams.

The multibeam coupling is relevant to calculations of both absolute growth or the convective TPD amplification. To interpret the experimental results described above, the convective gain was derived following the Rosenbluth method,^{14,31} which assumes that the common plasma wave propagates parallel to a linear density profile.

1. Multiple Linearly Polarized Beams

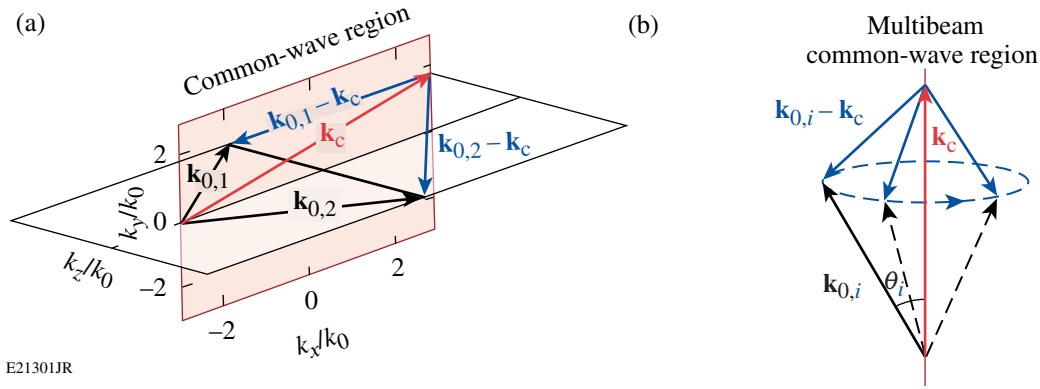
In the case of multiple laser beams driving a common electron plasma wave with frequency and wave vector (ω_c, \mathbf{k}_c), the dispersion relation for the common wave is $\omega_c^2 = \omega_{pe}^2 + 3\mathbf{k}_c^2 v_{\text{th},e}^2$ and for the corresponding daughter waves

$$(\omega_c - \omega_0)^2 = \omega_{pe}^2 + 3|\mathbf{k}_c - \mathbf{k}_{0,i}|^2 v_{\text{th},e}^2,$$

where $v_{\text{th},e}$ is the electron thermal velocity and ω_0 and $\mathbf{k}_{0,i}$ (with a magnitude k_0 independent of i) are the frequency and the wave vector of beam i . A common-wave region is defined where a resonant process exists and is determined by satisfying the dispersion relations for all laser beams and electron plasma waves leading to

$$\theta_i = \text{const}, \text{ for } i = 1 \dots n, \quad (1)$$

where θ_i is the angle between $\mathbf{k}_{0,i}$ and \mathbf{k}_c . All laser beams that drive a resonant common electron plasma wave must share the same angle with the common wave. For a two-beam configuration, Fig. 133.36(a) shows that this condition defines a plane in k space bisecting the wave vectors of the two laser beams. For more than two symmetrically oriented laser beams, Fig. 133.36(b) shows that this condition restricts the resonant common waves to a line.



E21301JR

Figure 133.36

(a) The common-wave region for two beams is given by a plane that bisects the wave vectors ($\mathbf{k}_{0,1}, \mathbf{k}_{0,2}$) of the laser beams (red plane). (b) A common electron plasma wave (EPW) can be driven only by multiple laser beams that share the same angle to the common-wave vector (θ_i) to satisfy the dispersion relation for each daughter EPW ($|\mathbf{k}_{0,i} - \mathbf{k}_c| = \text{const}$).

The dispersion relation for the common wave is derived following the TPD linear theory for the conditions where the collision frequency is much smaller than the growth rate

$$D(\omega_c, \gamma, |\mathbf{k}_c|) = - \sum_i \frac{(\gamma_{0,i}^2)^{\text{SB}}}{D(\omega_c - \omega_0, \gamma, |\mathbf{k}_c - \mathbf{k}_{0,i}|)}, \quad (2)$$

where the superscript SB refers to single beam, γ is the temporal growth rate,

$$D(\omega, \gamma, |\mathbf{k}|) = \left\{ \left[1 - \omega_{\text{pe}}^2 / \omega^2 (1 + 3k^2 \lambda_{\text{De}}^2) \right] \omega / 2 + i\gamma \right\}$$

is the dispersion relation, $\lambda_{\text{De}} = v_{\text{th},e} / \omega_{\text{pe}}$ is the Debye length, and ω_{pe} is the electron plasma frequency. The single-beam growth rate is given by $(\gamma_{0,i}^2)^{\text{SB}} = f_c (\gamma_{0,i}^2)_{\text{max}}^{\text{SB}} \cos^2 \alpha$, where α is the angle between the electric-field polarization vector and the common-wave vector and

$$f_c = \left[(k_c^2 - |\mathbf{k}_c - \mathbf{k}_0|^2) / k_0 |\mathbf{k}_c - \mathbf{k}_0| \right]^2.$$

The maximum single-beam growth rate squared is

$$(\gamma_{0,\text{max}}^2)^{\text{SB}} = 2 / (cn_e m_e) (k_0/2)^2 I_i,$$

where c is the light velocity, m_e is the electron mass, $n_c = m_e \omega_0^2 / 4\pi e^2$ is the critical density, and e is the electron charge.

To evaluate the maximum value of the growth rate, the minimum value of $D(\omega, \gamma, |\mathbf{k}_c - \mathbf{k}_{0,i}|)$ is determined by ensuring that the dispersion relations for all daughter

waves are satisfied [i.e., Eq. (1) is satisfied]. It follows that $D(\omega_c - \omega_0, \gamma, |\mathbf{k}_c - \mathbf{k}_{0,i}|) = \gamma = \text{const}$ and the temporal growth rate is given from Eq. (2) by

$$(\gamma_0^2)^{\text{MB}} = \sum_i (\gamma_{0,i}^2)^{\text{SB}}. \quad (3)$$

The common-wave growth rate is normalized to the maximum single-beam growth rate calculated for the overlapped intensity of the beams contributing to the common wave (I_Σ):

$$(\Gamma_0^2)^{\text{MB}} = \frac{(\gamma_0^2)^{\text{MB}}}{(\gamma_0^2)_{\text{max}}^{\text{SB}, I_\Sigma}} = f_c \sum_i \cos^2(\alpha_i) \beta_i, \quad (4)$$

where $\beta_i = I_i / I_\Sigma$, I_i is the intensity of the laser beam i , and α_i is the angle between the electric-field polarization vector and the common-wave vector. To determine the dominant common electron plasma wave, a maximum normalized growth rate $[(\Gamma_0^2)_{\text{max}}^{\text{MB}}]$ is calculated that depends only on the geometry and polarizations of the laser beams. The convective gain is given by

$$G_c = 6 \times 10^{-2} \frac{I_\Sigma L_n \lambda_0}{T_e} (\Gamma_0^2)_{\text{max}}^{\text{MB}}, \quad (5)$$

where I_Σ is in units of 10^{14} W/cm², L_n is in μm , T_e is in keV, and λ_0 is the laser wavelength in μm .

2. Multibeams with Polarization Smoothing

For more than two beams, the common-wave region defines a line [I_c displayed in Figs. 133.37(a) and 133.37(b)] and the growth rate for multiple beams is equal to the sum of the

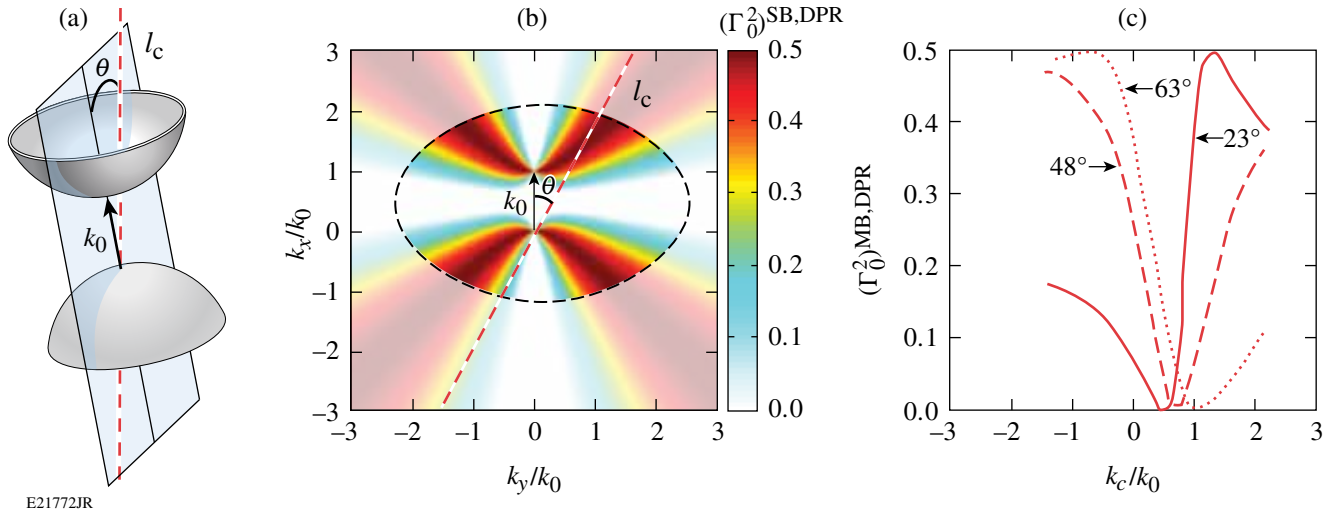


Figure 133.37

(a) A 3-D representation of the maximum growth rate for a single beam with polarization smoothing (gray hyperboloids). Multiple beams with polarization smoothing can couple through the common wave along the common-wave line (l_c , red dashed line) at an angle θ . (b) Normalized single-beam with polarization smoothing growth rate in the plane (\mathbf{k}_0, l_c). The Landau cutoff ($k\lambda_{De} = 0.25$, where k is the maximum value between k_c and $|\mathbf{k}_c - \mathbf{k}_0|$) for $T_e = 2$ keV is represented with a black dashed line. The normalized multibeam growth rate is equal to the single-beam growth rate along l_c . (c) Normalized multibeam growth rate calculated along the common-wave line for $\theta = 23^\circ$ (solid red line), $\theta = 48^\circ$ (dashed red line), and $\theta = 63^\circ$ (dotted red line). The cutoff for small and large \mathbf{k}_c corresponds to the Landau cutoff calculated for $T_e = 2$ keV.

growth rate for a single beam along this line [applying Eq. (3)]. Since the growth rate is azimuthally symmetric around \mathbf{k}_0 for each beam (Appendix A) and Eq. (1) must be satisfied, the growth rate along l_c is equal for each beam. The growth rate for multiple beams is given by the single-beam growth rate times the number of beams (N_Σ) that can drive the common wave $\left[(\gamma_0^2)^{\text{MB,PS}} = N_\Sigma (\gamma_0^2)^{\text{SB,PS}} \right]$. The multibeam growth rate is normalized to the maximum single-beam growth rate $\left[(\gamma_0^2)_{\text{max}}^{\text{SB,IS}} = N_\Sigma (\gamma_0^2)_{\text{max}}^{\text{SB,IS}} \right]$, resulting in a factor that depends only on the beam geometry

$$(\Gamma_0^2)^{\text{MB,PS}} = (\Gamma_0^2)^{\text{SB,PS}} = \frac{1}{2} f_c \sin^2 \theta. \quad (6)$$

To determine the maximum normalized growth rate, the common-wave line is plotted over the top of the single-beam growth rate calculated in the plane (\mathbf{k}_0, l_c) [Fig. 133.37(b)]. The multibeam normalized growth rate along the common-wave line is plotted in Fig. 133.37(c) for three angles. For most conditions, the common-wave line crosses the maximum normalized single-beam growth rate: for small values of θ [solid red curve in Fig. 133.37(c)], the common-wave line crosses the upper hyperbola and for large values of θ [dotted red line in Fig. 133.37(c)], the common-wave line crosses the lower hyperbola. In these two cases, the maximum normalized

multibeam growth rate with PS is $(\Gamma_0^2)_{\text{max}}^{\text{MB,PS}} = 0.5$. When the common-wave line does not intersect the hyperbola, the maximum normalized multibeam growth rate is slightly reduced [dashed red line in Fig. 133.37(c)]. The range of angles where the common-wave line does not cross the hyperbolas is given by the Landau cutoff and is, in general, small. The common-wave gain for multibeams with PS is given by

$$G_c^{\text{PS}} = 3 \times 10^{-2} \frac{I_\Sigma L_n \lambda_0}{T_e} \quad (7)$$

and, contrary to the gain in the case of polarized beams, does not depend on the geometry of the beams except as noted above. These results are consistent with the initial experiments that demonstrate multibeam effects on hot-electron generation.¹⁵

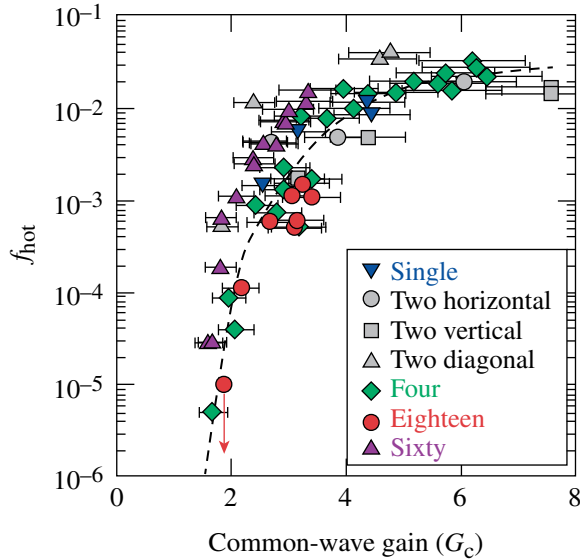
Interpretation of Experimental Results

In this section, the experimental results are discussed in the context of the common-wave model, where each experimental configuration was designed to vary a different parameter in the gain $\left[(\Gamma_0^2)_{\text{max}}^{\text{MB}}, N_\Sigma/N_{\text{beam}}, \text{ and } L_{n,q}/T_{e,q} \text{ (Table 133.VI)} \right]$. Figure 133.38 shows that the common-wave gain reproduces the measured hot-electron intensity thresholds shown in Fig. 133.35. For all laser-beam configurations, a gain threshold of ~ 2 is observed and a saturation is measured for $G_c \gtrsim 3$. This thresh-

Table 133.VI: List of parameters defining the common-wave gain that were varied during the experiments. N_Σ is the number of beams that share an equivalent angle with the common electron plasma wave [see Eq. (3)] with the largest growth rate, $L_{n,q}/T_{e,q}$ is in units of $\mu\text{m}/\text{keV}$; $(I_{\Sigma,q})_{\text{th}}^{\text{MB}}$ is in units of $10^{14} \text{ W}/\text{cm}^2$.

Configuration	N_{beam}	$(\Gamma_0^2)_{\text{max}}^{\text{MB}}$	N_Σ	$L_{n,q}/T_{e,q}$	$(I_{\Sigma,q})_{\text{th}}^{\text{MB}}$
Single	1	1.0	1	175	0.5
Two vertical	2	1.0	2	175	0.5
Two horizontal	2	0.8	2	175	0.7
Two diagonal	2	0.6	2	175	0.9
Four	4	0.5	4	175	1.1
Eighteen	18	0.5	6	135	1.4
Sixty	60*	0.5	6	60	3.1

*The number of beams that contribute in spherical geometry on OMEGA to the total overlapped intensity is ~ 20 .



E21699JR2

Figure 133.38
The hot-electron fraction is plotted as a function of the common-wave gain for each experimental configuration tested.

old is about $5\times$ lower than required for significant convective amplification from thermal noise. This discrepancy could be attributed to enhanced Langmuir wave noise, modified density profiles,³² or laser speckles.³³

The experimental results can be used to calculate an intensity threshold for hot-electron production from Eq. (5), when the convective gain is equal to 2, given by

$$(I_{\Sigma,q})_{\text{th}}^{\text{MB}} = \frac{94}{(L_{n,q}/T_{e,q})(\Gamma_0^2)_{\text{max}}^{\text{MB}}} \quad (8)$$

The intensity threshold for the different configurations is computed in Table 133.VI.

1. Beam Geometry and Polarization

On OMEGA EP, the maximum normalized growth rate was varied between the different configurations by changing the beam geometry and polarization while the other parameters remained constant (Table 133.VI). For the one- and two-beam configurations, a similar hot-electron production as a function of intensity is observed (Fig. 133.35). This demonstrates that for the two-beam configuration, the TPD is driven by a multi-beam process. For the four-beam configuration, the observed factor-of-2 increase in the intensity threshold (Fig. 133.35) is explained by the factor-of-2 decrease in the maximum normalized growth rate (Eq. 4) (Ref. 21).

The spectrum in k space where the normalized growth rate is maximum is larger for the single-beam configuration than for the two-beam configuration, whereas the maximum normalized growth rate is similar. The fact that the hot-electron fraction produced by the one-beam and two-beam configurations is similar suggests that the k -space volume of the large EPW's plays a minor role in the generation of hot electrons and that the hot-electron production depends, to first order, on the maximum normalized growth rate.

2. Number of Contributing Beams

In the 18-beam configuration on OMEGA, only a third of the beams contribute to the common-wave process, and the intensity that contributes to the maximum growth rate is reduced by 50% from the total overlapped intensity at the quarter-critical density. This is the primary explanation for the experimentally observed increase in the overlapped intensity threshold

(Fig. 133.35), where the beams are arranged in three cones of six at three different angles. As a result of the common-wave condition [Eq. (1)], each cone drives a different common wave and the coupling that dominates the TPD growth is the one with the largest growth rate. Since the beams were smoothed by polarization smoothing in this experiment, the coupling with the largest growth rate corresponds to the cone that has the highest intensity at the quarter-critical density. *LILAC* simulations indicate that the beams in the 23° cone have the highest intensity at the quarter-critical density ($I_{\Sigma,q}^{23^\circ} = 0.6 I_{\text{OVR},q}$, $I_{\Sigma,q}^{48^\circ} = 0.3 I_{\text{OVR},q}$, and $I_{\Sigma,q}^{63^\circ} = 0.1 I_{\text{OVR},q}$). This result is consistent with the experiments reported in Ref. 8, where the hot-electron generation was shown to depend only on the intensity of the beams of a single cone.

3. Plasma Parameters

The difference in the 18-beam and 60-beam thresholds observed in Fig. 133.35 is primarily a result of the difference in the plasma parameters, $L_{n,q}/T_{e,q}$ (Table 133.VI). For the spherical results, the maximum number of beams that are symmetrically oriented is six, arranged in a hexagon [a nine-beam coupling also exists but the large angle between the target normal and the beams (63°) significantly reduces their intensity at quarter-critical density]. As in the OMEGA planar experiments, the beams in the 23° cone produce the largest common-wave gain.

Conclusions

These experimental results indicate that the hot-electron threshold depends on the hydrodynamic parameters at the quarter-critical density, the configuration of the laser beams, and the sum of the intensity of the beams that share the same angle with the common-wave vector. A TPD model where multiple laser beams can share a common electron plasma wave has been presented. The resonant common-wave process occurs only when the multiple laser beams share the same angle with the common EPW. This creates a common-wave region where a maximum growth rate defines the dominant EPW, independent of the plasma conditions. To compare with the experimental results, the maximum common-wave growth rate is used to calculate a convective gain.

The experiments were designed to measure the threshold for hot-electron production while varying the different parameters [N_Σ , $(\Gamma_0^2)_{\text{max}}^{\text{MB}}$, I_s , L_n/T_e] in the common-wave gain. A significant increase in the hot-electron intensity threshold was observed when the maximum normalized growth rate was reduced by using four beams compared to one or two beams. A further reduction was observed when the number of beams that

can contribute to the common wave was reduced by distributing 18 beams into three cones. The overlapped intensity threshold was observed to be different for the various experimental configurations and is explained by the common-wave TPD model.

The common-wave theory is consistent with the initial experiments that first demonstrated multibeam effects on hot-electron generation.¹⁵ In these experiments, the hot-electron fraction was shown to be independent of the number of beams. The beams that were varied were from the same cone and therefore shared the same common plasma wave. These results can be applied to the indirect-drive experiments reported in Ref. 8 that showed the dependence of hot-electron generation on the intensity of the beams in a single cone.

ACKNOWLEDGMENT

This work was supported by the U.S. Department of Energy Office of Inertial Confinement Fusion under Cooperative Agreement No. DE-FC52-08NA28302, the University of Rochester, and the New York State Energy Research and Development Authority. The support of DOE does not constitute an endorsement by DOE of the views expressed in this article.

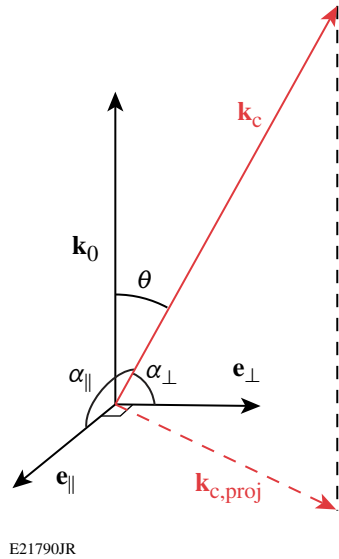
Appendix A: Single Beam with Polarization Smoothing

Polarization smoothing employs a birefringent crystal that separates the incident linearly polarized laser beam into two beams with orthogonal polarizations propagating at a slight angle ($\sim 40 \mu\text{rad}$) with respect to each other. The angle is small compared to the f number (25 mrad) of the laser beam so that the k -vectors of the two beams can be treated equivalently. From the normalized common-wave growth rate [Eq. (4)] and the fact that the intensity is equivalent between the two polarizations ($I_{\parallel} = I_{\perp} = I_{\Sigma}/2$), the normalized growth rate for a single beam with a PS is given by

$$\begin{aligned} (\Gamma_0^2)^{\text{SB,PS}} &= f_c \left[\frac{I_{\parallel}}{I_{\Sigma}} \cos^2(\alpha_{\parallel}) + \frac{I_{\perp}}{I_{\Sigma}} \cos^2(\alpha_{\perp}) \right] \\ &= 0.5 f_c \sin^2(\theta), \end{aligned} \quad (\text{A1})$$

where \parallel (\perp) refers to the parallel (perpendicular) polarized beam, and from Fig. 133.39, it is apparent that

$$\begin{aligned} \cos^2(\alpha_{\parallel}) + \cos^2(\alpha_{\perp}) &= \frac{(\mathbf{k}_c \cdot \mathbf{e}_{\parallel})^2 + (\mathbf{k}_c \cdot \mathbf{e}_{\perp})^2}{k_c^2} \\ &= \frac{\mathbf{k}_c^2}{k_c^2} = \sin^2 \theta, \end{aligned} \quad (\text{A2})$$



E21790JR

Figure 133.39

The projection of the common-wave vector \mathbf{k}_c in the plane $(\mathbf{e}_{\parallel}, \mathbf{e}_{\perp})$ for a single beam with a polarization smoothing (PS).

where \mathbf{e}_{\parallel} (\mathbf{e}_{\perp}) is the polarization vector of the parallel (perpendicular) polarized beam and $\mathbf{k}_{c,\text{proj}}$ is the projection of \mathbf{k}_c onto the plane $(\mathbf{e}_{\parallel}, \mathbf{e}_{\perp})$.

Equation (A1) shows that for a single beam with polarization smoothing, the growth rate in k space is symmetric around \mathbf{k}_0 (f_c depends only on $|\mathbf{k}_c|$, $|\mathbf{k}_0|$, and $|\mathbf{k}_c - \mathbf{k}_0|$). When \mathbf{k}_c is in the plane $(\mathbf{k}_0, \mathbf{e}_{\parallel})$, the term $\mathbf{k}_c \cdot \mathbf{e}_{\perp}$ cancels out and the normalized growth rate is simply equal to half the normalized growth rate for a beam with parallel polarization calculated in the polarization plane. Due to symmetry, the maximum growth rate is 0.5 and in k space defines two hyperboloids [Fig. 133.37(a)]. In each plane that contains \mathbf{k}_0 , the growth rate is equal to half the growth rate calculated for a linearly polarized single beam calculated in the polarization plane [Fig. 133.37(b)].

REFERENCES

1. J. Nuckolls *et al.*, *Nature* **239**, 139 (1972).
2. R. L. McCrory, D. D. Meyerhofer, R. Betti, R. S. Craxton, J. A. Delettrez, D. H. Edgell, V. Yu. Glebov, V. N. Goncharov, D. R. Harding, D. W. Jacobs-Perkins, J. P. Knauer, F. J. Marshall, P. W. McKenty, P. B. Radha, S. P. Regan, T. C. Sangster, W. Seka, R. W. Short, S. Skupsky, V. A. Smalyuk, J. M. Soures, C. Stoeckl, B. Yaakobi, D. Shvarts, J. A. Frenje, C. K. Li, R. D. Petrasso, and F. H. Séguin, *Phys. Plasmas* **15**, 055503 (2008).
3. J. D. Lindl *et al.*, *Phys. Plasmas* **11**, 339 (2004).
4. M. V. Goldman, *Ann. Phys.* **38**, 117 (1966).
5. C. S. Liu and M. N. Rosenbluth, *Phys. Fluids* **19**, 967 (1976).
6. A. Simon, R. W. Short, E. A. Williams, and T. Dewandre, *Phys. Fluids* **26**, 3107 (1983).
7. W. Seka, D. H. Edgell, J. F. Myatt, A. V. Maximov, R. W. Short, V. N. Goncharov, and H. A. Baldis, *Phys. Plasmas* **16**, 052701 (2009).
8. S. P. Regan, N. B. Meezan, L. J. Suter, D. J. Strozzi, W. L. Krueer, D. Meeker, S. H. Glenzer, W. Seka, C. Stoeckl, V. Yu. Glebov, T. C. Sangster, D. D. Meyerhofer, R. L. McCrory, E. A. Williams, O. S. Jones, D. A. Callahan, M. D. Rosen, O. L. Landen, C. Sorce, and B. J. MacGowan, *Phys. Plasmas* **17**, 020703 (2010).
9. D. W. Phillion *et al.*, *Phys. Rev. Lett.* **49**, 1405 (1982).
10. J. F. Myatt, J. Zhang, J. A. Delettrez, A. V. Maximov, R. W. Short, W. Seka, D. H. Edgell, D. F. DuBois, D. A. Russell, and H. X. Vu, *Phys. Plasmas* **19**, 022707 (2012).
11. R. Yan, C. Ren, J. Li, A. V. Maximov, W. B. Mori, Z. M. Sheng, and F. S. Tsung, *Phys. Rev. Lett.* **108**, 175002 (2012).
12. D. H. Froula, B. Yaakobi, S. X. Hu, P.-Y. Chang, R. S. Craxton, D. H. Edgell, R. Follett, D. T. Michel, J. F. Myatt, W. Seka, R. W. Short, A. Solodov, and C. Stoeckl, *Phys. Rev. Lett.* **108**, 165003 (2012).
13. *LLE Review Quarterly Report* **79**, 131, Laboratory for Laser Energetics, University of Rochester, Rochester, NY, LLE Document No. DOE/SF/19460-317, NTIS Order No. DE2002762802 (1999). (Copies may be obtained from the National Technical Information Service, Springfield, VA 22161.)
14. R. Yan, A. V. Maximov, C. Ren, and F. S. Tsung, *Phys. Rev. Lett.* **103**, 175002 (2009).
15. C. Stoeckl, R. E. Bahr, B. Yaakobi, W. Seka, S. P. Regan, R. S. Craxton, J. A. Delettrez, R. W. Short, J. Myatt, A. V. Maximov, and H. Baldis, *Phys. Rev. Lett.* **90**, 235002 (2003).
16. A. V. Maximov, J. Myatt, R. W. Short, W. Seka, and C. Stoeckl, *Bull. Am. Phys. Soc.* **52**, 195 (2007).
17. R. W. Short, *Bull. Am. Phys. Soc.* **53**, 245 (2008).
18. T. R. Boehly, D. L. Brown, R. S. Craxton, R. L. Keck, J. P. Knauer, J. H. Kelly, T. J. Kessler, S. A. Kumpan, S. J. Loucks, S. A. Letzring, F. J. Marshall, R. L. McCrory, S. F. B. Morse, W. Seka, J. M. Soures, and C. P. Verdon, *Opt. Commun.* **133**, 495 (1997).
19. J. H. Kelly, L. J. Waxer, V. Bagnoud, I. A. Begishev, J. Bromage, B. E. Kruschwitz, T. J. Kessler, S. J. Loucks, D. N. Maywar, R. L. McCrory, D. D. Meyerhofer, S. F. B. Morse, J. B. Oliver, A. L. Rigatti, A. W. Schmid, C. Stoeckl, S. Dalton, L. Folsbee, M. J. Guardalben, R. Jungquist, J. Puth, M. J. Shoup III, D. Weiner, and J. D. Zuegel, *J. Phys. IV France* **133**, 75 (2006).
20. D. H. Froula, D. T. Michel, I. V. Igumenshchev, S. X. Hu, B. Yaakobi, J. F. Myatt, D. H. Edgell, R. Follett, V. Yu. Glebov, V. N. Goncharov, T. J. Kessler, A. V. Maximov, P. B. Radha, T. C. Sangster, W. Seka, R. W. Short, A. A. Solodov, C. Sorce, and C. Stoeckl, *Plasma Phys. Control. Fusion* **54**, 124016 (2012).

21. D. T. Michel, A. V. Maximov, R. W. Short, S. X. Hu, J. F. Myatt, W. Seka, A. A. Solodov, B. Yaakobi, and D. H. Froula, *Phys. Rev. Lett.* **109**, 155007 (2012).
22. T. J. Kessler, Y. Lin, J. J. Armstrong, and B. Velazquez, in *Laser Coherence Control: Technology and Applications*, edited by H. T. Powell and T. J. Kessler (SPIE, Bellingham, WA, 1993), Vol. 1870, pp. 95–104.
23. T. R. Boehly, V. A. Smalyuk, D. D. Meyerhofer, J. P. Knauer, D. K. Bradley, R. S. Craxton, M. J. Guardalben, S. Skupsky, and T. J. Kessler, *J. Appl. Phys.* **85**, 3444 (1999).
24. P. B. Radha, T. J. B. Collins, J. A. Delettrez, Y. Elbaz, R. Epstein, V. Yu. Glebov, V. N. Goncharov, R. L. Keck, J. P. Knauer, J. A. Marozas, F. J. Marshall, R. L. McCrory, P. W. McKenty, D. D. Meyerhofer, S. P. Regan, T. C. Sangster, W. Seka, D. Shvarts, S. Skupsky, Y. Srebro, and C. Stoeckl, *Phys. Plasmas* **12**, 056307 (2005).
25. J. Delettrez, *Can. J. Phys.* **64**, 932 (1986).
26. B. Yaakobi, P.-Y. Chang, A. A. Solodov, C. Stoeckl, D. H. Edgell, R. S. Craxton, S. X. Hu, J. F. Myatt, F. J. Marshall, W. Seka, and D. H. Froula, *Phys. Plasmas* **19**, 012704 (2012).
27. B. Yaakobi, C. Stoeckl, T. Boehly, D. D. Meyerhofer, and W. Seka, *Phys. Plasmas* **7**, 3714 (2000).
28. B. Yaakobi, C. Stoeckl, W. Seka, J. A. Delettrez, T. C. Sangster, and D. D. Meyerhofer, *Phys. Plasmas* **12**, 062703 (2005).
29. C. Stoeckl, V. Yu. Glebov, D. D. Meyerhofer, W. Seka, B. Yaakobi, R. P. J. Town, and J. D. Zuegel, *Rev. Sci. Instrum.* **72**, 1197 (2001).
30. I. Kawrakow *et al.*, NRC, Ottawa, Canada, NRCC Report PIRS-701 (May 2011).
31. M. N. Rosenbluth, *Phys. Rev. Lett.* **29**, 565 (1972).
32. D. R. Nicholson and A. N. Kaufman, *Phys. Rev. Lett.* **33**, 1207 (1974).
33. G. Laval, R. Pellat, and D. Pesme, *Phys. Rev. Lett.* **36**, 192 (1976).